mathematics

Article

Statistical Image Watermark Algorithm for FAPHFMs Domain Based on BKF–Rayleigh Distribution

Siyu Yang , Ansheng Deng * and Hui Cui *

Information Science and Technology College, Dalian Maritime University, Dalian 116026, China; yangsy_1995@163.com
* Correspondence: ashdeng@dlmu.edu.cn (A.D.); cuihuilnnu@163.com (H.C.)

Abstract: In the field of image watermarking, imperceptibility, robustness, and watermarking capacity are key indicators for evaluating the performance of watermarking techniques. However, these three factors are often mutually constrained, posing a challenge in achieving a balance among them. To address this issue, this paper presents a novel image watermark detection algorithm based on local fast and accurate polar harmonic Fourier moments (FAPHFMs) and the BKF–Rayleigh distribution model. Firstly, the original image is chunked without overlapping, the entropy value is calculated, the high-entropy chunks are selected in descending order, and the local FAPHFM magnitudes are calculated. Secondly, the watermarking signals are embedded into the robust local FAPHFM magnitudes by the multiplication function, and then MMLE based on the RSS method is utilized to estimate the statistical parameters of the BKF–Rayleigh distribution model. Finally, a blind image watermarking detector is designed using BKF–Rayleigh distribution and LO decision criteria. In addition, we derive the closed expression of the watermark detector using the BKF–Rayleigh model. The experiments proved that the algorithm in this paper outperforms the existing methods in terms of performance, maintains robustness well under a large watermarking capacity, and has excellent imperceptibility at the same time. The algorithm maintains a well-balanced relationship between robustness, imperceptibility, and watermarking capacity.

Keywords: image watermarking; FAPHFM magnitudes; BKF–Rayleigh distribution model; LO decision criteria

MSC: 68-06

Citation: Yang, S.; Deng, A.; Cui, H. Statistical Image Watermark Algorithm for FAPHFMs Domain Based on BKF–Rayleigh Distribution. *Mathematics* **2023**, *11*, 4720. https://doi.org/10.3390/math11234720

Academic Editors: Kunpeng Liu, Pengfei Wang, Yifeng Gao and Yanjie Fu

Received: 28 October 2023
Revised: 13 November 2023
Accepted: 16 November 2023
Published: 21 November 2023

1. Introduction

With the rapid advancement of digital technology, the transmission of multimedia digital works over the Internet has become prevalent. This advancement has enabled the low-cost, high-speed reproduction and dissemination of digital media, leading to improved efficiency and accuracy in information expression and contributing to increased socio-economic benefits. However, this open Internet environment poses significant security threats and challenges for digital media resources. To address these challenges, digital watermarking has emerged as a promising solution for copyright protection and integrity authentication in open network environments. Digital watermarks, which are embedded within multimedia data, enable one to access, represent, manipulate, and distribute media without degrading its quality. As a result, digital watermarking technology finds extensive applications in various domains such as copyright protection, digital content authentication, anti-counterfeiting and traceability, broadcast monitoring, billing security, content management, and digital forensics. By employing digital watermarking technology, the feasibility of copyright protection and data integrity verification can be significantly improved, presenting a robust solution to the global issue of intellectual property protection.

Digital image watermarking technology is evaluated based on three crucial metrics: robustness, imperceptibility, and watermark capacity. There are mutual constraints among the three, so it is difficult to design a digital image watermarking algorithm that optimizes these three metrics simultaneously. Image watermarking algorithms are categorized into the spatial and frequency domains based on the embedding domain. The spatial-domain algorithm inserts the watermark data directly into the pixels of the original image. The method is simple to operate, but the robustness of the watermark is not sufficient to resist signaling attacks. In the frequency-domain algorithm, the watermark is embedded by changing the image transform domain coefficients. The robustness of the method is somewhat improved compared to null-domain watermark embedding. Some of the popular transforms include the wavelet family, such as the wavelet transform [1], discrete wavelet transform (DWT) [2,3], discrete cosine transform (DCT) [4], redundant discrete wavelet transform (RDWT) [5], dual-tree complex wavelet transform (DTCWT) [6], and integer wavelet transform (IWT) [7]; the contourlet family, such as the contourlet transform (CT) [8] and non-subsampled contourlet transform (NSCT) [9]; and the shearlet family, such as the discrete shearlet transform (DST) [10] and non-subsampled shearlet transform (NSST) [11]. In recent years, a novel watermarking method that considers the geometric invariance of images has emerged. This approach involves determining the geometric invariance of the carrier image before embedding and detecting the watermark. A breakthrough was achieved in 2000 when Alghoniemy et al. [12] applied image moments for the first time to image watermarking techniques.

There are many factors that affect the accuracy of watermark detection. In addition to the watermark carrier, they include the establishment of statistical models, the estimation of model parameters, and the construction method of the detector. The main statistical models commonly used are Gaussian distribution (GD) [13], generalized Gaussian distribution (GGD) [14], normal indicator distribution (NIG) [15], the Gaussian mixture model (GMM) [16], Bessel K-form (BKF) distribution [17,18], t location-scale (tLS) distribution [19], Cauchy distribution [20], Laplace distribution [21], and Weibull distribution [4]. However, a single distribution model cannot capture the correlation of coefficients at different scales and in different directions. Therefore, a single distribution model does not fit the coefficients well. In view of this, researchers have proposed joint statistical models, which have strong scale dependence and more fully consider the correlation between the coefficients. Common examples are multivariate Cauchy distribution (MCD) [9], the multivariate generalized Gaussian (MVGG) model [22], the hidden Markov model (HMM) [23], the Gaussian mixing-based vector hidden Markov tree model (HMTM) [24], the Cauchy mixture-based vector hidden Markov tree model [25], and the two-dimensional generalized autoregressive conditional heteroscedasticity (2D-GARCH) model [26]. Depending on the extraction requirements, watermarking algorithms can be categorized into watermark decoding [27–30] and watermark detection [4,31,32]. Watermark decoding is the extraction of watermark information at the receiver side, whereas watermark detection is the use of a binary decision criterion at the receiver side to determine whether the image contains watermark information or not. Watermark detection can be thought of as the detection of a signal in a noisy environment, where the coefficients represent the noisy environment and the watermark is the signal to be detected. The role of the detector is to detect the presence of hidden binary information in the observed image coefficients. The accuracy of parameter estimation also affects the performance of watermark detection. Currently, expectation maximization (EM) and maximum likelihood estimation (MLE) methods are widely used for the parameter estimation of statistical models. According to the presence or absence of the original medium in the detector, watermarking methods can be categorized into two main groups: blind watermarking and non-blind watermarking. In many practical applications, blind watermarking detectors are more applicable. In past studies, the decision rules for constructing detectors included the log-likelihood ratio test (LLRT) [15,19], RAO test [33], generalized likelihood ratio test (GLRT) [34], local maximum power (LMP) test [9], and log-likelihood ratio test (LRT) [21].

This paper focuses on exploring the issue of image copyright protection. Although digital watermarking technology has been widely used in the field of image copyright, there are still areas that need to be improved. First, regarding digital watermarking technology for copyright protection, the direct modification of the transform domain coefficients can satisfy the invisibility requirement, but it cannot effectively resist all kinds of attacks, so it is crucial to choose a more robust carrier to ensure the effectiveness of copyright protection. Secondly, a single distribution cannot effectively characterize the coefficient distribution and is not sufficient to resist stronger attacks, so choosing a joint statistical model can more accurately describe the coefficient distribution law. Thirdly, watermark information belongs to weak signals in non-Gaussian distributions, and a strong decision criterion is needed to improve the detection probability.

In this paper, an image watermarking algorithm based on BKF–Rayleigh distribution and the magnitudes of FAPHFMs is designed, which can still maintain good invisibility and robustness under a large watermarking capacity.

In summary, the contributions of this paper are as follows:

We take the magnitudes of FAPHFMs as the modeling object and provide a carrier object with higher robustness while ensuring imperceptibility.

We propose the BKF–Rayleigh distribution model, which can more accurately characterize the statistics of peaks and heavy tails and better capture the non-Gaussian distribution properties of the FAPHFM magnitudes.

We choose MMLE based on the RSS method to effectively solve the problem of model parameter estimation.

We construct a locally optimal detector based on BKF–Rayleigh distribution and the LO decision criterion to realize watermark detection.

Finally, we conduct many experiments to verify the advantages of the image watermark detector in this paper.

The remaining chapters are structured as follows: Section 2 focuses on statistical model-based digital image watermarking techniques in recent years. Section 3 briefly introduces the concept of FAPHFMs and investigates the robustness of FAPHFM magnitudes. Section 4 mainly studies the statistical characteristics of FAPHFM magnitudes and then fits the FAPHFM magnitude coefficients using the BKF–Rayleigh model. In order to improve the accuracy and reliability of the model, MMLE based on the RSS method is used to estimate the parameters of the BKF–Rayleigh model more accurately. In Section 5, we detail the embedding process of the watermarking algorithm. Section 6 derives the LO watermark detector based on the BKF–Rayleigh model and gives a detailed description of the performance of the new detection method. In Section 7, we analyze the detection probability of the proposed watermark detection method through a large number of simulation experiments and compare it with other excellent detectors. Section 8 is the conclusion.

2. Related Work

In this section, we introduce the relevant achievements of watermark detection techniques and watermark algorithms in the past few years. Chen et al. [35] used the Karush–Kuhn–Tucker (KKT) theorem to minimize the difference between the low-frequency coefficients of the DWT and the watermarked coefficients in order to modify the low-frequency amplitude of the watermark embedding. However, the obvious drawbacks and limitations of this system are its low robustness and low transparency. Moreover, the detection method in this system is semi-blind and faces implementation challenges in industrial applications. Amirmazlaghani [26] proposed a new additive image watermark detection method using the 2D-GARCH model to represent the wavelet coefficients and designed a watermark detector based on the 2D-GARCH model, which demonstrated excellent performance in experimental evaluations. However, the wavelet transform has limitations in 2D signals despite its high resolution in both the frequency and time domains. Etemad et al. [19] proposed a contourlet-domain multiplicative watermark detection method based on t-LS distribution, designed an optimal multiplicative watermark detector using the likelihood ratio decision rule and t position scale distribution, and derived the receiver operating characteristics. Kilari et al. [36] proposed a hybrid approach using the redundant discrete wavelet transform (RDWT) and digital image watermarking singular-value decomposition (SVD) schemes to provide authentication and security for aerial remote sensing images transmitted over the Internet. Three-level symmetric encryption with a low computational cost was used to ensure the security of the watermark. In order to obtain high-quality digital image watermarking results, an optimization algorithm based on hybrid locust-bat (G-BAT) soft computing (SC) was also proposed. The experimental results showed that the algorithm had high imperceptibility, robustness, embedding ability, and security when dealing with digital image watermarking for aerial remote sensing images. Zebbiche et al. [14] proposed a blind additive image watermarking scheme in the DTCWT domain. The high-frequency DTCWT coefficients were modeled using GG distribution, and the watermark detector was constructed based on RAO. The experimental results showed that the proposed algorithm was improved in terms of stealth, detection accuracy, and robustness to common attacks. However, RAO hypothesis testing requires sufficiently large amounts of sample data to achieve optimal asymptotic performance, which greatly increases the computational cost. As aviation technology continues to advance, aerial remote sensing images also need to be protected. Hu et al. [32] proposed a watermark detection method based on a non-parametric model. They used kernel density estimation (KDE) and non-parametric detection to model the speech frame coefficients of a tertiary DWT, designed a maximum likelihood (ML) detector during the watermark detection process, and used the Neyman–Pearson criterion to calculate the decision threshold. Experiments showed that the algorithm had good steganography performance and robustness. However, this algorithm was only applicable to a small sample size, which limited its usefulness. Oswaldo et al. [37] proposed a copyright protection and information transmission algorithm. This algorithm utilized histogram distortion caused by embedding strategies and introduced a new histogram position function method to display any watermark of sufficient quality to be recognized or decoded by any application. Ahmaderaghi et al. [21] proposed a DST-based blind watermarking algorithm for images. The maximum likelihood detection algorithm was implemented using the Neyman–Pearson criterion for the Laplace model of DST coefficients under certain assumptions. Gong et al. [38] designed a new watermarking scheme with higher concealment performance and robustness to enhance the imperceptibility of the watermark by selecting the watermark insertion region through Canny edge detection. During the watermark embedding process, the robustness of the digital watermarking scheme was further improved due to the stability of the additional threshold and singular-value decomposition. The experimental results showed that the watermarking scheme outperformed other typical watermarking schemes in terms of imperceptibility and robustness. Niu et al. [39] proposed a blind statistical color image watermarking scheme based on Cauchy–Rayleigh distribution and the LMP decision criteria, introduced the MLE method to estimate the parameters of the statistical model of Cauchy–Rayleigh distribution, and subsequently developed a blind color image watermarking detector using the Cauchy–Rayleigh statistical model and the LMP decision criteria. Numerous experiments demonstrated the excellent performance of the proposed method in all aspects. Wang et al. [9] proposed a locally optimal image watermark detector based on the NSCT domain. Using the LMP decision criteria rule and RSS-based Cauchy distribution, an optimal multiplicative watermarking detector was proposed, and a statistical model was used to derive a closed-form expression for the watermarking detector. The experimental results showed that the watermarking algorithm was highly efficient and provided better steganography performance. Amini et al. [24] proposed a novel sparse-domain color image watermarking algorithm and its corresponding detector. They used a hidden Markov model to consider the correlation between RGB channels and the interscale correlation of the sparse coefficients of color images and designed an effective detector to check the existence of watermarks by establishing a binary hypothesis test. Experiments showed that the proposed detector provided a higher detection rate and exhibited better performance in terms of robustness. In the context of advancing medical technology, the protection of copyright for medical images has gained great importance.

Huang et al. [40] proposed a robust zero watermarking algorithm designed specifically for medical images, which employed DTCWT, Hessenberg decomposition, and the multilevel discrete cosine transform (MDCT), in addition to combining cryptographic algorithms, third-party concepts, and chaotic sequences to encrypt watermarked images in order to improve their security. By utilizing the zero watermarking technique, the algorithm ensured the integrity, robustness, and concealment of medical images. The algorithm was effective in extracting watermarked images and was resistant to various attacks. In recent years, deep neural networks (DNNs) have gained popularity in the field of digital watermarking, with researchers exploring their potential for watermark embedding and detection [41,42]. Pavlović et al. [43] utilized deep neural networks for the robust digital watermarking and authentication of speech signals, employing two neural networks, the employer and the detector. The embedding networks achieved imperceptible watermark embedding by minimizing the difference between the original and watermarked signals, and the detector could always detect watermarks without error, even if its input was a signal that had been attacked multiple times.

Several moment-based image watermarking algorithms are described below. Hosny et al. [44] proposed a new robust watermarking algorithm for color images by deriving new fractional-order multichannel orthogonal exponent moments (MFrEMs) and their invariants for geometric transformations. A new robust color image watermarking algorithm was constructed using these high-precision moments, and the experimental results showed that the proposed robust watermarking algorithm outperformed existing algorithms in terms of visual imperceptibility and robustness to various attacks. Wang et al. [45] proposed GPHFMs based on geranion theory and polar harmonic Fourier moments (PHFMs) and used them for light-field image watermarking, which effectively solved the problem of weak resistance to geometric attacks commonly found in existing light-field image watermarking schemes. Gong et al. [46] proposed a robust color image watermarking algorithm with geometric correction by LS-SVR based on low-order quaternion fractional-order orthogonal Fourier–Mellin moments (QFrOOFMMs). In most cases, the algorithm outperformed typical algorithms in resisting both common and geometric attacks, but there was still room for improvement in terms of computational accuracy. Yamni et al. [47] proposed a watermarking algorithm for digital image copyright protection based on fractional Charlier–Meixner moments (FrCMMs), which embedded watermarks into FrCMM coefficients, thus improving invisibility, robustness, and security. Wang et al. [48] proposed a robust zero watermark algorithm based on MZMs (modified Zernike moments) to resist geometric attacks. Firstly, MZMs were constructed by improving the radial basis function of ZMs (Zernike moments), and then a robust zero watermark algorithm to resist geometric attacks was proposed, which could achieve the lossless copyright protection of images.

3. Robustness Analysis of the FAPHFM Magnitudes

3.1. Fast and Accurate Polar Harmonic Fourier Moments (FAPHFMs)

If a gray image in polar coordinates is $f(\rho,\theta)$, then the fast and accurate polar harmonic Fourier moments (FAPHFMs) on the unit circle can be expressed as [49]

$$P_{nm} = \frac{2}{\pi}\sum_{u}\sum_{v}\left[\sum_{i=0}^{8} f_i(\rho_{uv},\theta_{uv})\left(H_{nm}(\rho_{uv},\theta_{uv})^1 + jH_{nm}(\rho_{uv},\theta_{uv})^2\right)\right] \tag{1}$$

where $f_i(\rho_{uv},\theta_{u,v})$ denotes the pixel values of the eight symmetry points corresponding to each ring in the polar coordinate sector grid. Moreover, there exist

$$\begin{cases} H_{nm}(\rho_{uv},\theta_{uv})^1 = H'_{nm}(\rho)cos(m\theta) \\ H_{nm}(\rho_{uv},\theta_{uv})^2 = H'_{nm}(\rho)sin(m\theta) \end{cases} \tag{2}$$

The original image can be approximately reconstructed using the formula below:

$$\tilde{f}(x,y) = \sum_{n=0}^{K} \sum_{m=-n}^{K} \tilde{P}_{nm} H_n(r_{xy}) exp(-jm\theta_{xy}) \tag{3}$$

3.2. Analysis of the Magnitudes of FAPHFMs

Due to the geometric invariance, low time complexity, and high noise immunity of FAPHFMs, we chose the magnitudes of the FAPHFMs as the embedding position of the watermark. First, the original image with pixels of 512×512 is segmented into 8×8 non-overlapping sub-blocks; then, the fifth-order FAPHFM transform is applied to each block to obtain the FAPHFM magnitudes of the image. Figure 1 shows the fifth-order transforms of different images with a size of 340×192.

(**a**) Lena

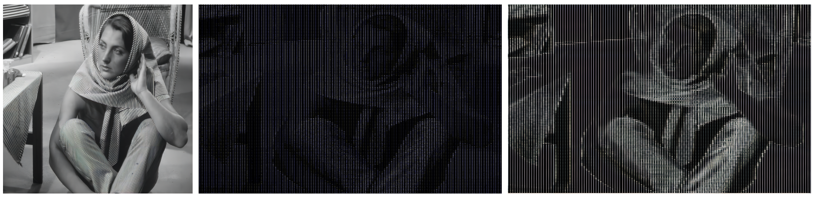

(**b**) Barbara

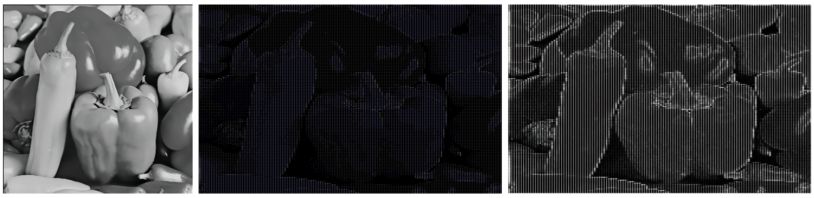

(**c**) Peppers

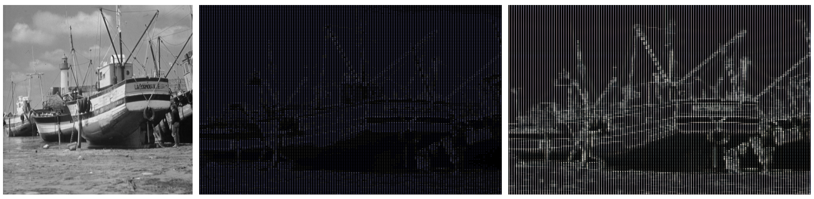

(**d**) Boat

Figure 1. Original images and FAPHFM magnitude images (original images on the left, FAPHFM magnitude images in the center, and FAPHFM magnitude images ($\times 10$) on the right).

In order to verify the robustness and applicability of the FAPHFM magnitudes, we introduce the concept of the normalization error. The most common normalization method is data Z-score normalization, which maps the data uniformly into the interval $[0, 1]$. The normalization error is denoted as

$$P = |I - I_{attack}| \tag{4}$$

where I_{attack} is the attacked signal and I is the original signal.

$$E = \frac{1}{n} \sum_{i}^{n} \left| \frac{P - \mu}{\sigma} \right| \tag{5}$$

where n is the number of attack signals, μ is the mean of P, and σ is the standard deviation of P.

Table 1 presents the normalized error values for the original and FAPHFM magnitude images under various attacks. The test images are referred to as Lena, Barbara, and Peppers.

Table 1. The error normalization between the original image and the attacked image.

Attack Type	Lena		Barbara		Peppers	
	FAPHFM Magnitudes	**Host Image**	**FAPHFM Magnitudes**	**Host Image**	**FAPHFM Magnitudes**	**Host Image**
JPEG compression $QF = 90$	0.0142	0.0521	0.0154	0.0502	0.0175	0.0564
JPEG compression $QF = 30$	0.0187	0.0769	0.0173	0.0836	0.0191	0.0832
Median filtering 9×9	0.0107	0.0287	0.0186	0.0364	0.0122	0.0253
Median filtering 5×5	0.0101	0.0232	0.0154	0.0337	0.0096	0.0121
Gaussian filtering 9×9	0.0126	0.0293	0.0298	0.0465	0.0134	0.0303
Gaussian filtering 5×5	0.0103	0.0244	0.0159	0.0324	0.0113	0.0226
Gamma correction $\gamma = 0.9$	0.0224	0.0375	0.0237	0.0405	0.0287	0.0398
Gamma correction $\gamma = 2$	0.0414	0.0649	0.0426	0.0627	0.0408	0.0619

It is well known that the smaller the normalization error value, the less significant and more robust the difference between the attacked image and the original image. Figure 2 shows the normalized-error images obtained using the Lena, Barbara, Peppers, and Boat test images under various attacks. The left side of the figure shows the normalized-error images based on the original images, and the right side shows the normalized-error images based on the magnitudes of the FAPHFMs. The darker the color of the image, the smaller the normalization error value.

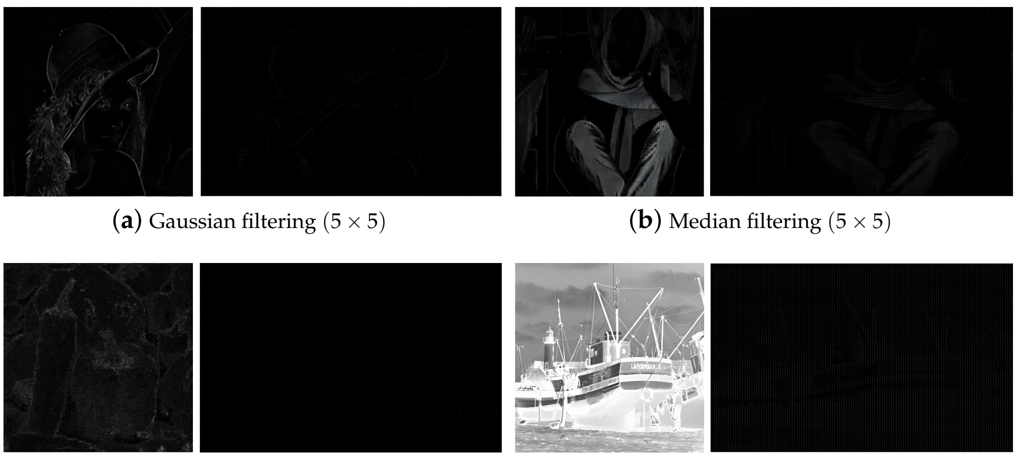

(**a**) Gaussian filtering (5×5) (**b**) Median filtering (5×5)

(**c**) JPEG $(QF = 50)$ (**d**) Gamma correction $\gamma = 2$

Figure 2. Normalized-error images under various attacks.

Based on the analysis in Table 1, it can be concluded that the normalization error of the FAPHFM magnitude coefficients is smaller than the normalization error of the original images. In addition, as shown in Figure 1, the normalization-error image of the FAPHFM magnitudes is darker compared to the original images. Both subjective and objective results indicate that the FAPHFM magnitudes are more robust than the original images. Therefore, in this paper, the local FAPHFM magnitudes are selected as the embedding location of the watermarking information.

4. Modeling the Magnitudes of FAPHFMs

4.1. Statistical Analysis of the FAPHFM Magnitudes

Studying the distribution characteristics of the FAPHFM magnitudes is one of the key steps for accurate modeling. In this paper, we take four typical grayscale images as an example and analyze the edge statistical characteristics of the FAPHFM magnitudes using distribution histograms and kurtosis values. In the experiment, the test image of size 512×512 is divided into 8×8 non-overlapping sub-blocks of size 64×64, and then the FAPHFM magnitudes of each image block are calculated, resulting in a total of 4096 moments values. The histograms of these moment values are given in Figure 3. It is clear from the histograms that the magnitude coefficients distributed on the positive half-axis of the x-axis are mainly distributed near zero, and the farther away from zero, the smaller the coefficients, with the magnitude coefficients of the FAPHFMs being characterized by spiky and heavy tails. The kurtosis values are 36.7894, 26.7264, 32.0963, and 21.0022, much larger than 3 (the kurtosis of Gaussian distribution), which indicates that the magnitude coefficients show non-Gaussian distribution. Therefore, a reasonable model is needed to accurately characterize the magnitude coefficients. The standard grayscale images used in this section are from the CVG-UGR database.

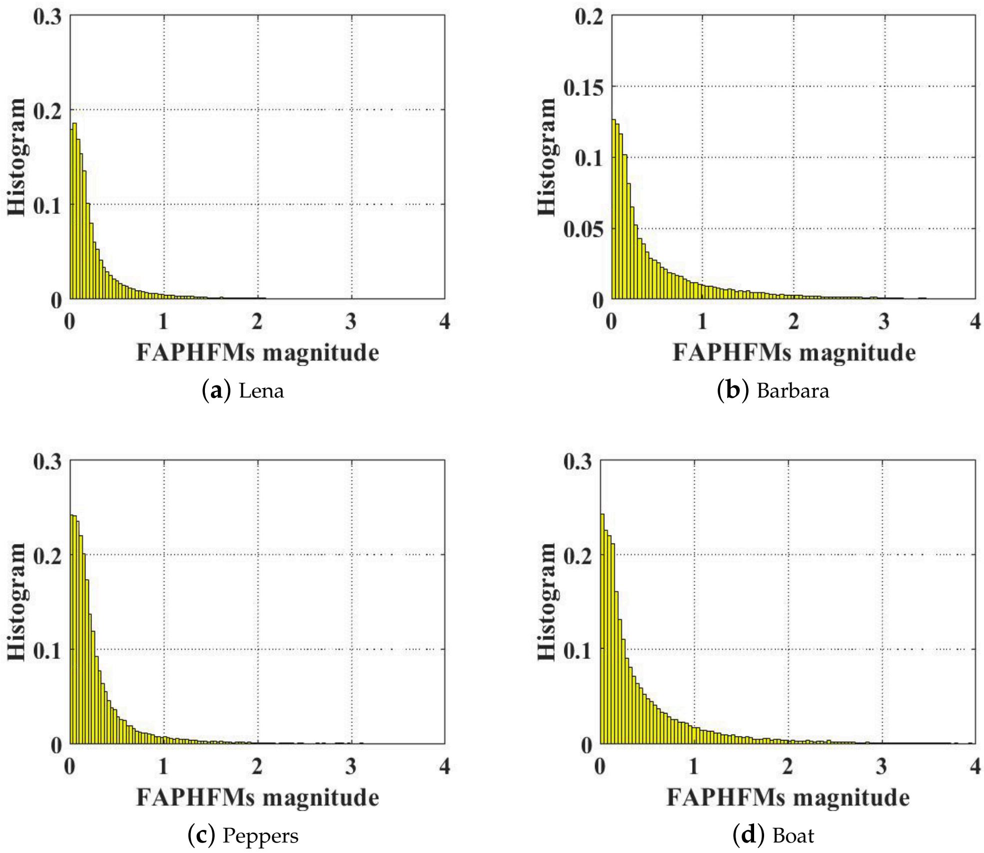

(**a**) Lena (**b**) Barbara (**c**) Peppers (**d**) Boat

Figure 3. Distribution histograms of FAPHFM magnitude coefficients.

4.2. Statistical Modeling of FAPHFM Magnitudes

In the current field of statistical modeling, most models are usually described via a single probability density function (PDF). However, the use of a single probability distribution assumes independence between the coefficients and ignores the strong correlation that exists between the coefficients in the modeling process. This simple modeling approach has low computational complexity and poor modeling accuracy. BKF distribution, also known as Bessel K-distribution, has gained popularity in various research fields due to its superior data fitting ability. This model can effectively capture the interdependence between coefficients, which greatly improves the descriptive ability of the image [50]. Rayleigh distribution is a subclass of lifetime distribution and a type of Weibull distribution with a shape parameter of 2. It has a wide range of applications in the fields of radiocommunication engineering and engineering measurements. It is commonly used to characterize the statistical time-varying properties of the received envelope of a flat fading signal or independent multipath components [51]. In order to improve the modeling accuracy and capture the distributional characteristics of the FAPHFM magnitude coefficients more effectively, the BFK–Rayleigh distribution model is proposed in this study. The model comprehensively reflects the statistical characteristics of FAPHFM magnitudes.

Let $X = \{x_1, x_2, \ldots, x_m\}$ and $Y = \{y_1, y_2, \ldots, y_m\}$ be random variables obeying the distribution of the BKF–Rayleigh model. The fit plot is defined as follows:

$$f(X,Y) = \frac{2\alpha}{\Gamma(z_1, z_2)} e^{-(z_1 x_m + z_2 y_m)} \sqrt{\frac{1}{2}} x_m \left(1 - e^{-(z_1 x_m + z_2 y_m)}\right) \tag{6}$$

where Γ denotes the gamma function, α is the scale parameter, and z_1 and z_2 are the shape parameters.

The Kolmogorov–Smirnov (K-S) test is an effective method for testing whether an empirical distribution conforms to a known theoretical distribution, and its core is based on the cumulative distribution function (CDF). The expression for the K-S test is as follows:

$$Q_{ks} = max|C_e(x) - C_t(x)| \tag{7}$$

where $C_e(x)$ is the empirical cumulative distribution function, and $C_t(x)$ is the reference cumulative distribution function. The smaller the K-S value, the better the fit of the distribution function used.

In order to verify the ability of BKF–Rayleigh distribution to characterize the fringe properties of the FAPHFM magnitude coefficients, K-S tests were performed on each of the four images in this paper. Table 2 records the K-S values of the FAPHFM magnitude coefficients with different theoretical distributions. It can be seen that the K-S value of BKF–Rayleigh distribution was the smallest, which indicates that BKF–Rayleigh distribution was able to accurately characterize the edge features of the FAPHFM magnitude coefficients and outperformed the other models.

Table 2. Comparison of K-S values of various statistical distributions.

Image	Rayleigh Distribution	BKF Distribution	Cauchy Distribution	Weibull Distribution	Cauchy–Rayleigh Distribution	BKF–Rayleigh Distribution
Lena	0.0466	0.0521	0.0642	0.2135	0.0864	0.0202
Barbara	0.0457	0.0574	0.0576	0.3013	0.0953	0.0186
Peppers	0.0514	0.0493	0.0507	0.2341	0.0821	0.0124
Boat	0.0485	0.0471	0.0497	0.2414	0.0954	0.0203

In order to analyze the performance of BFK–Rayleigh distribution more intuitively, the modeling results of the four image magnitude coefficients with different distribution models are recorded in Figure 4. A comparison shows that the fitting degree of the BFK–Rayleigh distribution model was higher than that of the other distribution models. Therefore, it can be concluded that the BFK–Rayleigh distribution model more accurately describes the magnitude coefficients of FAPHFMs.

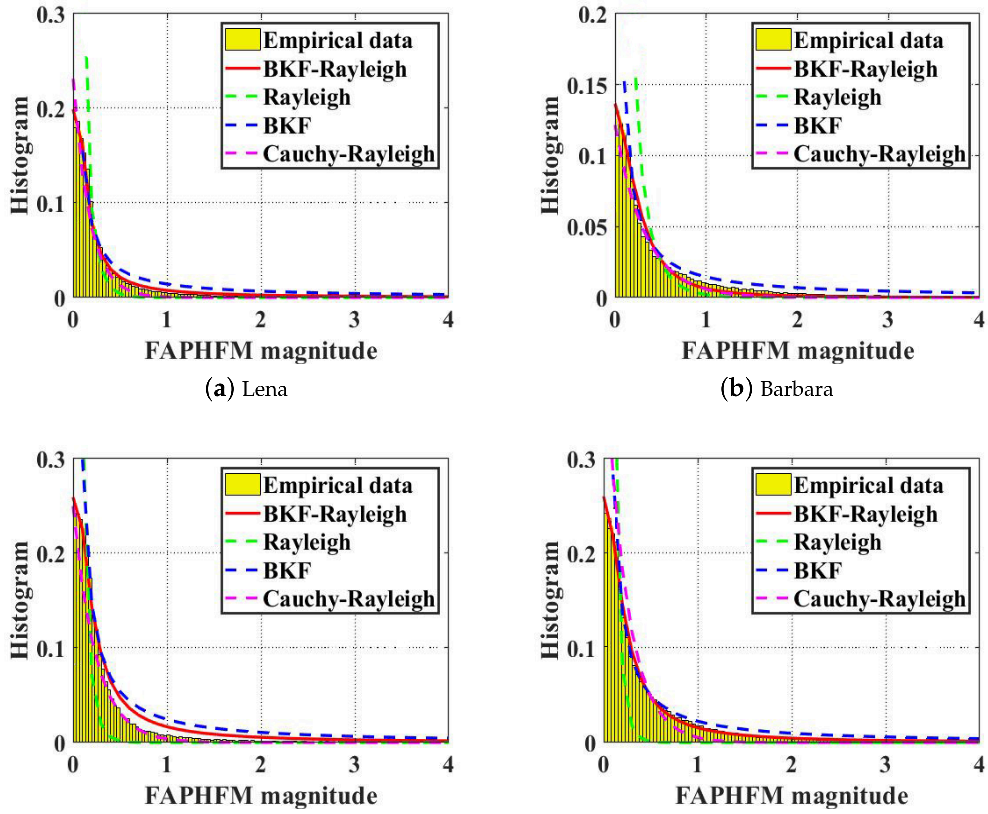

(**a**) Lena (**b**) Barbara (**c**) Peppers (**d**) Boat

Figure 4. Fitting diagrams of FAPHFM magnitude coefficients.

4.3. Model Parameter Estimation

Parameter estimation plays a vital role in statistical modeling watermarking techniques, and accurate parameter values can ensure the performance of the watermark detector. Compared with maximum likelihood estimation (MLE) based on ranked set sampling (RSS), modified maximum likelihood estimation (MMLE) based on the RSS method is more robust and efficient for location parameter estimation and has lower time complexity [52]. In this paper, we use MMLE based on RSS for the parameter estimation of the BFK–Rayleigh distribution model.

MMLE based on RSS is described as follows:

$$T_m(x) = \left(\frac{2\sum_{i=1}^{m}(m-i+1)x_{i(i)}^2}{m^2+3m} \right)^{\frac{1}{2}} \tag{8}$$

where x_i is the sorted set of samples, and m is the sorted capacity.

Defining $X = \{x_1, x_2, \ldots, x_m\}$ and $Y = \{y_1, y_2, \ldots, y_m\}$ as two sets of training samples, the parameter values of the BFK–Rayleigh model are estimated as follows:

(1) The log-likelihood function of the BFK–Rayleigh distribution model is determined as

$$\ln L(\alpha, z_1, z_2) = -\frac{\sqrt{2}}{2} \ln \frac{2\alpha}{\Gamma(z_1, z_2)} \cdot (z_1 x_m + z_2 y_m) x_m + \ln \frac{2\alpha}{\Gamma(z_1, z_2)} \cdot (2z_1 x_m + 2z_2 y_m) \tag{9}$$

The training samples are sorted in ascending order:

$$x_1 \leq x_2 \leq \cdots \leq x_m \tag{10}$$

$$y_1 \leq y_2 \leq \cdots \leq y_m \tag{11}$$

(2) The function $g(x_i, y_i) = e^{(z_1 x_m z_2 y_m)}$ is obtained by implementing a Taylor series expansion at the point (t_i, r_i):

$$\begin{aligned} g(x_i, y_i) &= g(t_i, x_i) + \left.\frac{\partial g(x_i, y_i)}{\partial x_i}\right|_{t_i, r_i} + (y_i - t_i)\left.\frac{\partial g(x_i, y_i)}{\partial y_i}\right|_{t_i, r_i} \\ &\cong e^{-(z_1 t_i + z_2 t_i)} \cdot [(-z_1)(x_i - t_i) + (-z_2)(y_i - t_i)] \end{aligned} \tag{12}$$

(3) Finally, the likelihood equation is solved, and a unique solution is obtained with the following results for parameters α, z_1, and z_2:

$$\frac{\partial \ln(\alpha, z_1, z_2)}{\partial \alpha} = -\frac{\sqrt{2}}{2\alpha} \cdot g(x_i, y_i) x_m + \sum_{i=1}^{m} \frac{2}{\alpha} \cdot g(x_i, y_i) \tag{13}$$

$$\frac{\partial \ln(\alpha, z_1, z_2)}{\partial z_1} = -\frac{\sqrt{2}}{2z_1} \cdot g(x_i, y_i) x_m + \sum_{i=1}^{m} \ln \frac{2\alpha}{\Gamma(z_1, z_2)} \cdot 2x_m \tag{14}$$

$$\frac{\partial \ln(\alpha, z_1, z_2)}{\partial z_2} = -\frac{\sqrt{2}}{2z_2} \cdot g(x_i, y_i) x_m + \sum_{i=1}^{m} \ln \frac{2\alpha}{\Gamma(z_1, z_2)} \cdot 2x_m \tag{15}$$

Numerical solutions for the parameters are obtained by equating the above equation to 0.

Monte Carlo simulation experiments were conducted to compare the performance of MMLE based on the RSS method with commonly used MMLE methods. The findings verified the superior performance of MMLE based on the RSS method in terms of both time complexity and parameter estimation accuracy. In our experiments, we used the inverse distribution function method to generate discrete random variables that obeyed the shape parameter $z_1 = 1$. For the estimation of the shape parameter z_2, this experiment generated 1000 random sets of random variables under each shape parameter z_2 for 1000 sampling experiments. When the random sample size was 5000, the average estimates and average error values calculated by the two parameter estimation methods are presented in Table 3.

Table 3. The average estimated results of shape parameter z_2.

Actual Shape Parameter z_2	MMLE Based on RSS		MMLE	
	Average Error	Average Estimated Value	Average Error	Average Estimated Value
5.0	0.0113	5.0113	0.0184	4.9816
4.0	0.0101	4.0101	0.0159	4.0159
3.0	0.0086	2.9914	0.0138	3.0138
2.0	0.0071	1.9929	0.0112	1.9888
1.0	0.0054	1.0054	0.0089	1.0069

Figure 5 illustrates the comparison of the average error and average running time between MMLE based on the RSS method and the MMLE method.

The following conclusions can be drawn from Table 3 and Figure 5: the larger the sample size, the smaller the average error of the parameter estimates, but the longer the average running time. This is due to the small sample problem in statistical theory, whereby it is difficult to represent the totality adequately with a small sample, leading to limitations in the accuracy and reliability of the estimates. As the sample size increases, the computational time increases accordingly. In the simulation experiments, for different sample sizes, MMLE based on the RSS parameter estimation method showed better performance, and compared with the MMLE method, MMLE based on RSS parameter estimation had lower time complexity. Therefore, in this paper, MMLE based on the RSS method was chosen to obtain the parameters of the BFK–Rayleigh statistical model.

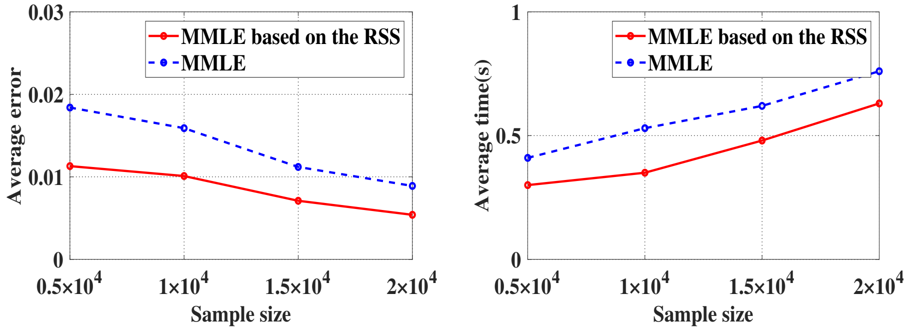

(**a**) Average errors (**b**) Average times

Figure 5. A comparison of results between the two methods under different sample sizes.

5. Digital Watermark Embedding

The image digital watermarking technique studied in this paper comprises two parts: watermark embedding and watermark detection. This section mainly introduces the watermark embedding process, which uses the multiplicative method to embed the watermark information in the magnitudes of the FAPHFMs with local geometric invariance. Algorithm 1 gives the pseudo-code for watermark embedding.

Algorithm 1 Watermark embedding algorithm

Input: Original I, watermark information w;
Output: Watermarked image I';
1: Image segmentation 8×8;
2: High-entropy block selection by Equation (16);
3: FAPHFM magnitude;
4: Magnitude moment selection;
5: Multiplicative watermark embedding by Equation (17);
6: Watermarked image block;
7: Watermarked image I';
8: **return** I'.

$I = \{f(x,y), 0 \leq x \leq N, 0 \leq y \leq N\}$ represents the original carrier image, where $f(x,y)$ represents the image pixel; $w = \{w_l \in \{-1,1\}, 1 \leq l \leq L\}$ represents the binary watermark bit; and $I' = \{f(x,y), 0 \leq x \leq N, 0 \leq y \leq N\}$ represents the image with a watermark.

Step 1: Original image segmentation. The original carrier image is segmented into individual non-overlapping sub-blocks of size 64×64, and the N sub-blocks are sorted by the entropy value. Entropy (H) [53] is a stochastic statistical scale that can be used to describe the texture of an image. High-entropy regions are rich in textural features and are therefore suitable for anti-noise and facilitating information hiding. Using the entropy masking model, we can effectively obtain invisible watermarked images. We calculate the entropy value of all image blocks and sort the N sub-blocks in descending order according to the entropy value:

$$H = -\sum_{j=1}^{J} p(a_j) \cdot logp(a_j) \tag{16}$$

where a_j represents a discrete set of possible events whose probability is expressed as $p(a_j)$, and J represents the number of possible events.

Step 2: The selection of high-entropy blocks and watermark embedding. The first M high-entropy blocks $A_l (l = 1, 2, 3, \ldots, L)$ are selected, and the magnitude coefficients based on the fifth-order FAPHFMs are computed for each high-entropy block. The target point

(5, 5) of the magnitude coefficient block is changed by the multiplication rule to embed the watermark sequence w_l so that each magnitude is embedded with the same watermark bit. The embedding expression is as follows:

$$y_i = \begin{cases} x_i \cdot (1 + \lambda w_l) \text{ if } w_l = 1, \\ x_i \cdot (1 - \lambda w_l) \text{ if } w_l = -1. \end{cases} \quad i \in A_l \tag{17}$$

where y_i represents the moment value containing the watermark; x_i denotes the original moment value; and λ represents the embedding strength, which plays a crucial role in balancing the imperceptibility and robustness of the watermark and takes a value of $0 \leq \lambda \leq 1$ in general. λ is computed by the watermark document ratio (WDR). The formula is as follows:

$$WDR = 10log_{10}(\frac{\lambda^2 \sigma_w^2}{\sigma_i^2}) \tag{18}$$

where σ_w^2 is the variance of the watermark sequence, and σ_i^2 is the variance of the moment value of the original image.

We rewrite the above formula as

$$\lambda = \sqrt{10^{\frac{WDR}{10}} \times \sigma_i^2} \tag{19}$$

Step 3: Obtaining the watermark image block. The formula for an image block containing watermark information is as follows:

$$f_e(x,y) = f(x,y) - f_r(x,y) + f_{e'}(x,y) \tag{20}$$

where $f(x,y)$ denotes an image block of original FAPHFMs, $f_{e'}(x,y)$ denotes a reconstructed image block of FAPHFMs containing watermarks, and $f_r(x,y)$ denotes a reconstructed image block of original FAPHFMs.

Step 4: Obtaining a watermarked image. The high-entropy image block with a watermark is exchanged with the original image block to obtain the image I' with a watermark.

6. Digital Watermark Detection

The purpose of watermark detection is to determine whether an image contains watermark information or not, and in recent years, a variety of detection methods have been developed based on the statistical properties of the moment coefficients, which have proven to be effective in obtaining accurate and reliable detection results. In this section, a novel image watermark detector is proposed using FAPHFM magnitude coefficients and the BFK–Rayleigh model. The detection process incorporates the LMP to improve the detection performance.

6.1. Locally Optimal Watermark Detector

When the watermark embedding strength is weak, watermark detection can be considered as a weak signal detection problem. Conversely, when the watermark strength is high, it can be viewed as a strong signal detection problem. Given that the watermark strength is usually weakened by attacks such as noise, rotation, and filtering, detecting a strong watermark signal can also be considered as detecting a relatively small signal. In detection theory, the local maximum potential (also known as the local optimum, LO) test is considered to be the best detection method for weak signals in non-Gaussian environments. It minimizes the detection error. Considering that the watermark information is usually very weak, the watermark detector based on the LMP decision criterion is asymptotically optimal for weak signals.

To determine the presence of watermark information, the watermark detection process at the receiving end typically follows binary hypothesis theory, where H_0 denotes that there is no watermark information in the image, H_1 denotes that the image contains watermark information, x is the original FAPHFM magnitude coefficient, y is the watermark-containing

FAPHFM magnitude coefficient, $W = \{w_i \in \{-1, 1\}, 1 \leq i \leq L\}$ is the L-bit watermark signal, and λ is the embedding strength:

$$\begin{aligned} H_0 &: y = x \\ H_1 &: y = x \cdot (1 + \lambda W) \end{aligned} \tag{21}$$

The likelihood ratio $\Lambda(Y)$ designed according to the Neyman–Pearson (NP) criterion is as follows:

$$\Lambda(Y) = \frac{f_Y(y \mid H_1)}{f_Y(y \mid H_0)} \underset{H_0}{\overset{H_1}{\gtrless}} \eta \tag{22}$$

where $\Lambda(Y)$ denotes the likelihood ratio, and η denotes the detection threshold. $f_Y(y|H_0)$ and $f_Y(y|H_1)$ are the conditional probability density functions under the two hypotheses. If $\Lambda(Y) > \eta$, H_1 exists; otherwise, H_0 exists. In practical applications, the log-likelihood is generally more commonly used than the likelihood ratio, and the log-likelihood ratio expression is

$$l(Y) = \ln[\Lambda(Y)] = \sum_{i=1}^{L} \ln \frac{f_Y(y_i \mid H_1)}{f_Y(y_i \mid H_0)} \underset{H_0}{\overset{H_1}{\gtrless}} \tau \tag{23}$$

where $\tau = \ln(\eta)$.

The Taylor series expansion of the above equation at $\lambda = 0$ according to the LMP decision criterion is

$$\begin{aligned} l(y_x)|_\lambda &= l(y_x)|_{\lambda=0} + \left.\frac{\partial l(y_x)}{\partial \lambda}\right|_{\lambda=0} \cdot \lambda + o(\lambda) \\ &\cong g_{LO}(y_x) \cdot \lambda + o(\lambda) \\ &= g_{LO}(x_i) \cdot \lambda \end{aligned} \tag{24}$$

where $g_{LO}(x_i)$ denotes the locally optimal non-linearity and is expressed according to the BKF–Rayleigh model:

$$g_{Lo}(x_i) = \frac{\frac{\partial f_X(y_x)}{\partial y_x}}{f_X(y_x)} = \frac{(1-2\alpha) - x_m e^{-(z_1 x_m + z_2 y_m)}}{\sqrt{2}\alpha - e^{-(z_1 x_m + z_2 y_m)}} \tag{25}$$

The final detector expression is

$$\begin{aligned} l(g_{LO}(Y)) &= \textstyle\sum_{i=1}^{L} g_{LO}(y_x) \cdot \lambda \\ &= \textstyle\sum_L \frac{\lambda w_i (1-2\alpha) - x_m e^{-(z_1 x_m + z_2 y_m)}}{\sqrt{2}\alpha - e^{-(z_1 x_m + z_2 y_m)}} \underset{H_0}{\overset{H_1}{\gtrless}} \tau \end{aligned} \tag{26}$$

where Y denotes the vector value of the FAPHFM magnitudes of the locally optimal BKF–Rayleigh model, and $g_{LO}(Y)$ denotes the output value.

When $l(g_{LO}(Y)) > \tau$, the detector at the receiving end determines that the image contains a watermark, and when $l(g_{LO}(Y)) < \tau$, the detector at the receiving end determines that there is no watermark. Here, y_x denotes the magnitude coefficients of the FAPHFMs embedded with watermark information, and $g_{LO}(y_x)$ denotes the inverse function of H_1 under assumptions.

Under the H_0 hypothesis, the mean m_0 and variance σ_0^2, respectively, are expressed as follows:

$$m_0 = E[g_{Lo}(Y) \mid H_0] = E\left[\sum_{i=1}^{L} \frac{\lambda w_i(1-2\alpha) - x_m e^{-(z_1 x_m + z_2 y_m)}}{\sqrt{2}\alpha - e^{-(z_1 x_m + z_2 y_m)}}\right] = 0 \tag{27}$$

$$\begin{aligned}\sigma_0^2 &= \text{var}[g_{Lo}(Y) \mid H_0] \\ &= E\left[\left(\sum_{i=1}^{L} \frac{\lambda w_i(1-2\alpha) - x_m e^{-(z_1 x_m + z_2 y_m)}}{\sqrt{2}\alpha - e^{-(z_1 x_m + z_2 y_m)}}\right)^2\right] \\ &= \sum_{i=1}^{L}\left[\left(\frac{\lambda w_i(1-2\alpha) - x_m e^{-(z_1 x_m + z_2 y_m)}}{\sqrt{2}\alpha - e^{-(z_1 x_m + z_2 y_m)}}\right)^2\right]\end{aligned} \tag{28}$$

Under the H_1 hypothesis, the mean m_1 and variance σ_1^2, respectively, are expressed as follows:

$$\begin{aligned}m_1 &= E[g_{Lo}(Y) \mid H_1] \\ &= E\left[\sum_{i=1}^{L} \frac{\lambda w_i(1-2\alpha) - x_m e^{-(z_1 x_m + z_2 y_m)}}{\sqrt{2}\alpha - e^{-(z_1 x_m + z_2 y_m)}}\right] \\ &= \sum_{i=1}^{L}\left[\frac{\lambda w_i(1-2\alpha) - (x_m + \lambda x_m) e^{-(z_1(x_m + \lambda y_m) + z_2(x_m + \lambda y_m))}}{\sqrt{2}\alpha - e^{-(z_1(x_m + \lambda y_m) + z_2(x_m + \lambda y_m))}}\right]\end{aligned} \tag{29}$$

The above equation can be simplified to obtain

$$x_1 = \frac{\lambda w_i(1-2\alpha)}{\sqrt{2}\alpha - e^{-(z_1(x_m + \lambda y_m) + z_2(x_m + \lambda y_m))}} \tag{30}$$

$$x_2 = \frac{(x_m + \lambda x_m) e^{-(z_1(x_m + \lambda y_m) + z_2(x_m + \lambda y_m))}}{\sqrt{2}\alpha - e^{-(z_1(x_m + \lambda y_m) + z_2(x_m + \lambda y_m))}} \tag{31}$$

$$m_1 = \sum_{i=1}^{L}(x_1 + x_2) \tag{32}$$

$$\sigma_1^2 = \text{var}(g_{Lo}(Y) \mid H_1) = E\left[\sum_{l=1}^{L}(x_1 + x_2)^2\right] \tag{33}$$

6.2. Watermark Detection

The pseudo-code for watermark detection is shown in Algorithm 2.

Step 1: Similar to the embedding process, watermarked image I' is segmented into N non-overlapping sub-blocks of size 64×64, and the N sub-blocks are sorted in descending order according to the entropy value.

Step 2: For high-entropy block selection, the first M high-entropy blocks A_m $(m = 1, 2, 3, \ldots, M)$ are selected, and the magnitude coefficients based on the fifth-order FAPHFMs are computed for each high-entropy block. The detector is constructed for the magnitudes of the FAPHFMs containing watermarks.

Step 3:The characteristics are analyzed, and MMLE based on the RSS method is used to estimate the magnitudes of the FAPHFMs containing watermarks.

Step 4: According to the decision criterion, an expression based on the BKF–Rayleigh distribution model is derived to construct the watermark detector, which ultimately determines whether or not the image contains watermarked information based on the threshold value.

Algorithm 2 Watermark detection algorithm

Input: Watermarked image I';
Output: Containing watermark information w_1, no watermark information w_1;

Image segmentation 8×8;
High-entropy block selection by Equation (16);
FAPHFM magnitude;
Magnitude moment selection;
MMLE based on RSS by Equation (8);
Threshold value selection;
Construction of LO detector;
if $l(g_{LO}(Y)) > \tau$ **then**
    w_1;
else
    w_0;
end if
return w_0 or w_1.

6.3. Performance Analysis of Watermark Detector

It is crucial to analyze the performance of watermark detection methods before practical application. The probability of a false alarm P_{fa} and the probability of detection P_{det} are two important metrics for image watermark detection algorithms. P_{fa} is the probability that the detector incorrectly detects a watermark in the absence of a watermark, and P_{det} is the probability that the detector successfully detects a watermark if the image contains a watermark. P_{fa} and P_{det}, respectively, are defined as follows:

$$\begin{aligned} P_{fa} &= P(l_{LO}(Y) > \tau \mid H_0) \\ &= P\left(\frac{l_{LO}(Y)}{\sigma_0} > \frac{\tau - m_0}{\sigma_0}\right) \\ &= Q\left(\frac{\tau - m_0}{\sigma_0}\right) \end{aligned} \tag{34}$$

$$\begin{aligned} P_{det} &= P(l_{\mathrm{LO}}(Y) > \tau \mid H_1) \\ &= P\left(\frac{l_{LO}(Y)}{\sigma_1} > \frac{\tau - m_1}{\sigma_1}\right) \\ &= Q\left(\frac{\tau - m_1}{\sigma_1}\right) \end{aligned} \tag{35}$$

where $Q(x) = \frac{1}{\sqrt{2\pi}} \int_x^{+\infty} e^{-t^2/2} dt$; m_0 and σ_0 represent the mean and variance, respectively, under hypothesis H_0; and m_1 and σ_1 represent the mean and variance, respectively, under hypothesis H_1. The expression of threshold τ is

$$\tau = m_0 + \sigma_0 Q^{-1}(P_{fa}) \tag{36}$$

Watermark detection at the receiver side can be achieved by incorporating the LO statistic $g_{LO}(Y)$ and threshold τ into the equation. Combined with Equations (34) and (35), the expression for the receiver operating characteristic (ROC) is as follows [54]:

$$\begin{aligned} P_{det} &= Q\left(\frac{\tau - \mu_1}{\sigma_1}\right) \\ &= Q\left(\frac{\sigma_0}{\sigma_1} Q^{-1}\left(P_{fa}\right) - \frac{\mu_1 - \mu_0}{\sigma_1}\right) \end{aligned} \tag{37}$$

ROC curves can be plotted with respect to P_{fa} and P_{det} according to Equation (37) and can be used to subjectively judge the performance of the watermark detector. In addition, an objective judgment of the detector's performance can be achieved by calculating the area under the receiver operating characteristic curve (AUROC), which takes values in the range [0, 1] [55]. The AUROC can reflect the relationship between P_{fa} and P_{det}. For a given P_{fa}, the smaller the false-alarm probability P_m, the larger the P_{det} value $(P_{det} = 1 - P_m)$. In other words, the higher the AUROC value, the better the detection performance of the detector.

7. Experimental Results

In this section, the performance of the image watermarking algorithm proposed in this paper is tested and compared with that of other image watermarking algorithms through detailed experiments. In the performance tests, we evaluated the algorithm in terms of imperceptibility, robustness, watermarking capacity, time complexity, and accuracy degree in comparison with other state-of-the-art watermark detection schemes. All the experiments were implemented in MATLAB R2022a, with a personal computer configured with a Windows 10 system and Intel(R) Xeon (R) CPU i7-3470 @ 3.20 GHz 8 GB RAM.

The test images used in this study were all standard grayscale images of size 512 × 512 from a standard image database. The digital watermarks were generated by pseudo-random sequences, and each watermark bit was represented by 1 or −1.

7.1. Watermark Detector Performance Evaluation

7.1.1. Accuracy

The theoretical ROC curve can be used to measure the performance of a detector and needs to be close to the empirical ROC curve to prove its validity. In order to validate the theoretical expression of the proposed detection method, the theoretical ROC curve and the empirical ROC curve were compared by simulation experiments. We selected 96 standard grayscale images of size 512 × 512 from the standard test image database. In the Monte Carlo simulation experiment, 100 binary watermarking sequences with a length of 4000 bits were randomly generated. The experiments were set to take values of $[10^{-8} \le P_{fa} \le 10^{-2}]$, with a WDR ranging from −42 dB to −48 dB. Figure 6 presents the average of the theoretical and empirical ROC curves. We could observe that the two ROC curves basically overlapped, which indicated that the theoretical mean and variance of the LO statistic were accurate. This validated the effectiveness of the theoretical ROC curves for subsequent testing.

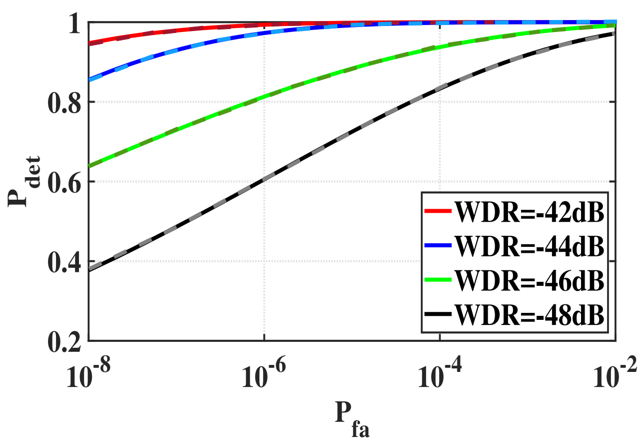

Figure 6. Theoretical ROC curves (solid lines) and empirical ROC curves (dotted lines).

7.1.2. Imperceptibility

Imperceptibility is an important metric for watermarking algorithms, and the peak signal-to-noise ratio (PSNR) is a widely accepted criterion for quantifying image imperceptibility. The test results of the imperceptibility of this algorithm are given in Figure 7. In this experiment, 5000-bit pseudo-random sequences were embedded into a standard grayscale image with a size of 512 × 512 pixels. The WDR was −42 dB in the experiment. As shown in Figure 7b, the naked eye could not recognize an obvious difference between the watermarked image and the original image. Figure 7c shows the differences between the original image and the watermarked image, which was enlarged by 10 times in this paper for the sake of clarity. The PSNRs of this algorithm were 49.5441, 47.7812, 46.2466, and 47.8112, all greater than 38, indicating that the proposed algorithm had good imperceptibility.

(**a**) Original images

(**b**) Watermarked images

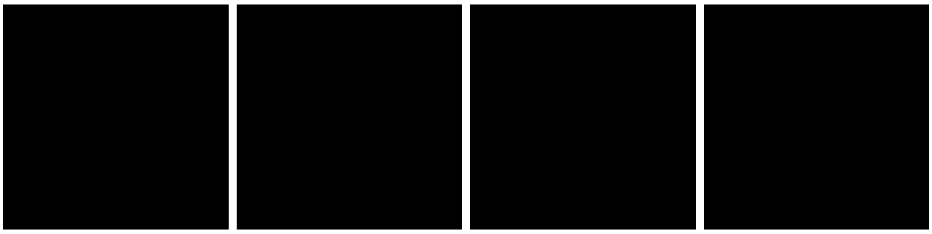

(**c**) Differences in the images (×10)

Figure 7. Imperceptibility analysis.

7.1.3. Robustness

In order to assess the robustness of the algorithms in this paper, we plotted the following line graphs using the LO statistic $g_{LO}(Y)$ and the threshold τ to reflect the responsiveness of the detector under different attacks. Figure 8a shows the detection response under JPEG compression attack with a quality factor (QF) ranging from 10 to 100. Figure 8b shows the detection response based on Gaussian filtering, with the window sizes of 3×3, 5×5, and 7×7. Figure 8c shows the detection response for clipping, with values of 2%, 5%, 10%, 15%, and 20%. Figure 8d demonstrates the detection response under the attack of additive white Gaussian noise (AWGN) with σ_n values of 5 to 35. The experimental results show that the LO detector in this paper always maintained accurate detection under different kinds of attacks with different intensities, indicating the strong robustness of the detector.

7.1.4. Capacity and Time

Watermarking capacity is an important metric for evaluating digital image watermarking algorithms. Usually, increasing the watermarking capacity will reduce the imperceptibility of the watermarked image and increase the time complexity of the algorithm. Therefore, an excellent watermarking algorithm should have improved robustness without affecting the imperceptibility of the watermarked image and try to expand the watermarking capacity. In the experiments, watermark sequences of different lengths were embedded into 20 standard grayscale images with sizes of 512×512 pixels, and the WDR was set to −42 dB. The relationship between the average PSNR, the average watermark embedding/detection time, and the watermarking capacity is shown in Tables 4–6. From the tables, it can be seen that the image watermarking algorithm proposed in this paper achieved and maintained good imperceptibility and ensured a sufficient watermark capacity. In addition, the embedding and detection time of the watermarking algorithm was relatively short.

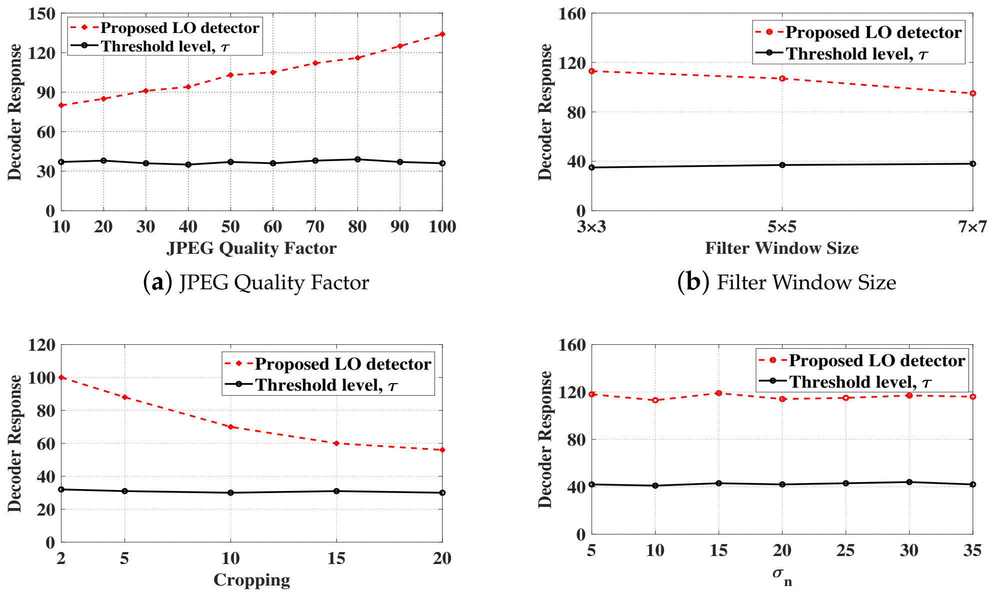

(**a**) JPEG Quality Factor (**b**) Filter Window Size

(**c**) Cropping (**d**) AWGN

Figure 8. The detection responses for the Lena image.

Table 4. Objective PSNR values under different watermark capacities.

Watermark Capacity	Lena	Barbara	Peppers	Boat
1000	52.3469	51.6486	52.8765	51.4642
5000	50.2632	48.5375	49.1576	48.9754
10,000	48.3165	45.2492	47.2481	46.3571

Table 5. The watermark embedding time of the proposed scheme.

Watermark Capacity	Lena	Barbara	Peppers	Boat
1000	2.3642	2.5413	2.6715	2.3429
5000	3.2566	3.3611	3.2691	3.3615
10,000	4.4125	4.5429	4.3153	4.4362

Table 6. The watermark detection time of the proposed scheme.

Watermark Capacity	Lena	Barbara	Peppers	Boat
1000	2.5424	2.3125	2.1537	2.2153
5000	3.4698	3.2147	3.3243	3.1245
10,000	4.3142	4.2593	4.1244	4.7233

Table 7 gives the PSNR values under different watermarking capacities. By comparing the results, it can be found that the PSNR of the proposed algorithm was slightly lower than that of other methods presented in the literature [56] when the watermarking capacity was 1000 bits, and our algorithm's PSNR was the highest when the watermarking capacity was increased to 5000 or 10,000 bits. This proves that our algorithm still had good imperceptibility under the premise of ensuring a larger watermarking capacity.

Table 7. Objective PSNR values for different algorithms.

Watermark Capacity	Literature [57]	Literature [56]	Literature [58]	Proposed
1000	50.1634	52.6166	51.2947	52.3469
5000	47.6129	49.4824	48.3342	50.2632
10,000	44.3462	45.1937	43.1673	48.3165

7.2. Comparison with State-of-the-Art Methods

In this section, the superiority of the watermark detection scheme proposed in this paper is further verified by comparison with Cauchy–Rayleigh [39], BGWM-HMT [59], and CHMM [24] distribution schemes. The same test images and experimental parameters were used in the experiments.

7.2.1. Probability of Detection for Varying Watermark Strengths

This section focuses on comparing the detection probabilities of the four algorithms at different embedding strengths. In the experiment, $P_{fa} = 10^{-2}$, and the test images were the grayscale Lena, Barbara, Peppers, Boat, Airplane, and Couple images with sizes of 512×512 pixels. Figure 9 shows the detection probability line graph of the different detection algorithms under different WDRs. It can be clearly seen from the graph that as the watermark embedding strength increased, the detection efficiency of the detector also improved. It is noteworthy that our detection algorithm always maintained a high detection probability under different WDRs.

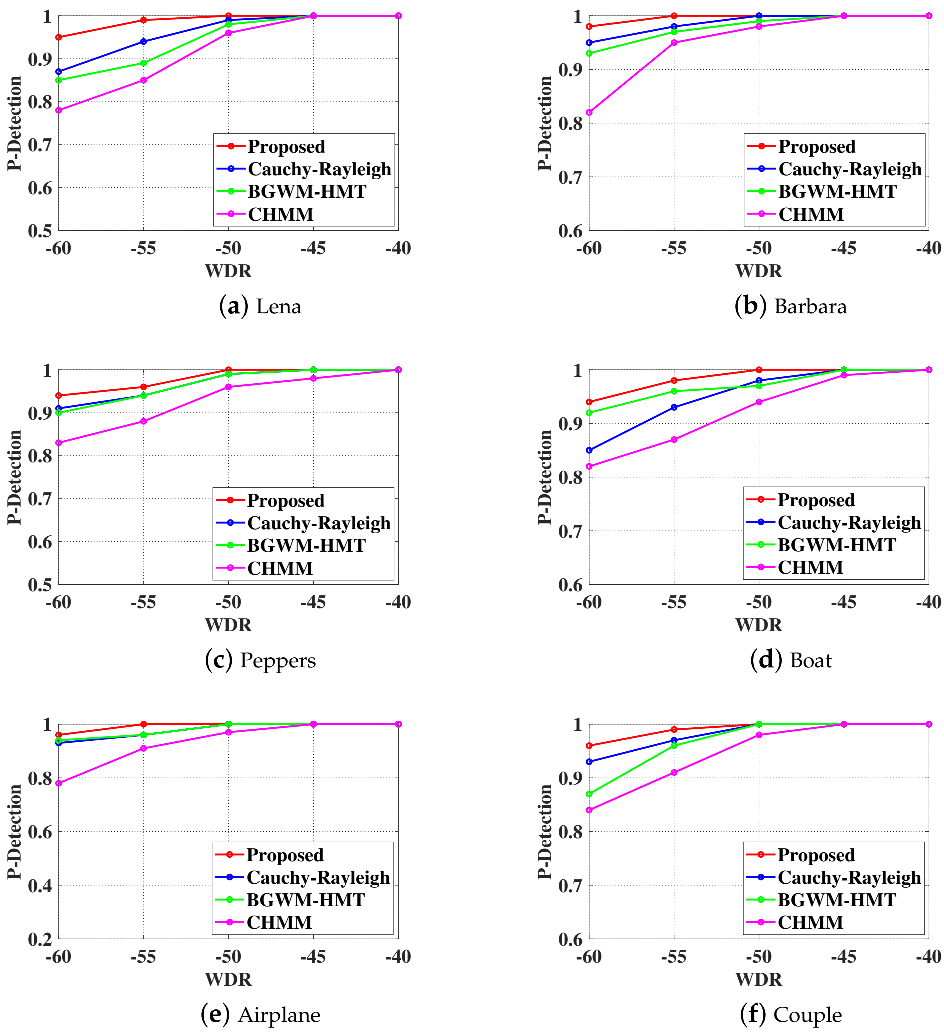

(**a**) Lena (**b**) Barbara (**c**) Peppers (**d**) Boat (**e**) Airplane (**f**) Couple

Figure 9. Comparison of detection probability results under different WDR values.

7.2.2. AUROC Values under Various Attacks

In this section, we compare the detector proposed in this paper with detectors using Cauchy–Rayleigh distribution, BGWM-HMT distribution, and CHMM distribution. Twenty-four grayscale images of size 512 × 512 with WDR = −42 dB, $P_{fa} = 10^{-2}$, and a watermark sequence length of 1000 bits were selected for 100 experiments. The average AUROC values of the 24 experimental images are given in Table 8. The results show that the detector proposed in this paper consistently obtained the highest AUROC values compared to the other detectors, i.e., the detector proposed in this paper surpassed other detectors in terms of performance and effectiveness.

Table 8. The AUROC values of different detectors without attacks.

Methods	CHMM	BGWM-HMT	Cauchy–Rayleigh	Proposed
AUROC	0.9964	0.9971	0.9978	0.9989

To clearly demonstrate the robustness of the algorithm proposed in this paper, Figure 10 gives the average AUROC test results of our detector and other existing detectors under various attacks. Figure 10a evaluates the robustness of the detectors under JPEG compression with the quality factor (QF) set in the range of 5 to 35. As the QF increased, the detection performance of all the detectors improved. It is noteworthy that the detector proposed in this paper exhibited stronger robustness compared to the other detectors. Figure 10b investigates the performance of the detector under additive white Gaussian noise (AWGN) attack. The proposed detector had the largest AUROC value among all the detection algorithms under AWGN attack. The proposed detector had the largest AUROC value among all the detection algorithms when $\sigma = 40$, and it consistently obtained the highest AUROC value. When evaluating the performance of any watermarking method, salt and pepper noise and Gaussian noise are considered common attacks. As can be seen in Figure 10c,d, salt and pepper noise and Gaussian noise consistently resulted in an AUROC value above 0.95 for our detector, which indicates that our detector had excellent noise immunity. Shear is a common geometric attack. Figure 10e evaluates cropping, another common geometric attack. Our detector exhibited high detection performance, with all AUROC values remaining above 0.9, highlighting its robustness to cropping attacks. Figure 10f shows the AUROC values under gamma correction, which is a method designed to increase the accuracy of the representation of darker image values while decreasing the accuracy of brighter image values; the tested detector maintained a high detection performance.

In Table 9, we compare the watermark detection performance of our detector with that of the CHMM [24] and Cauchy–Rayleigh [39] detectors. Twenty images with 512 × 512 pixels were used as carrier images, and the comparison experiments were carried out under the same experimental conditions, where $P_{fa} = 10^{-2}$.

Table 9. Average AUROC values under various attacks.

Attack Type		CHMM	Cauchy–Rayleigh	Proposed
Median filtering (3 × 3)	WDR = −50 dB	0.9367	0.9549	0.9623
	WDR = −45 dB	0.9511	0.9862	0.9987
Gaussian filtering (3 × 3)	WDR = −45 dB	0.9476	0.9714	0.9754
	WDR = −40 dB	0.9643	0.9942	0.9992
JPEG compression (QF = 30)	WDR = −55 dB	0.9014	0.9422	0.9535
	WDR = −50 dB	0.9376	0.9716	0.9847
AWGN $\sigma_n = 10$	WDR = −50 dB	0.9422	0.9843	0.9843
	WDR = −45 dB	0.9589	0.9877	0.9962
Salt and pepper noise (0.01)	WDR = −45 dB	0.9676	0.9843	0.9981
	WDR = −40 dB	0.9755	0.9936	0.9993
Rotation 0.5°	WDR = −45 dB	0.9284	0.9743	0.9891
Rotation 1°	WDR = −45 dB	0.8866	0.9578	0.9772
Scaling 0.5	WDR = −45 dB	0.9128	0.9416	0.9846
Scaling 2	WDR = −45 dB	0.7934	0.8423	0.9614

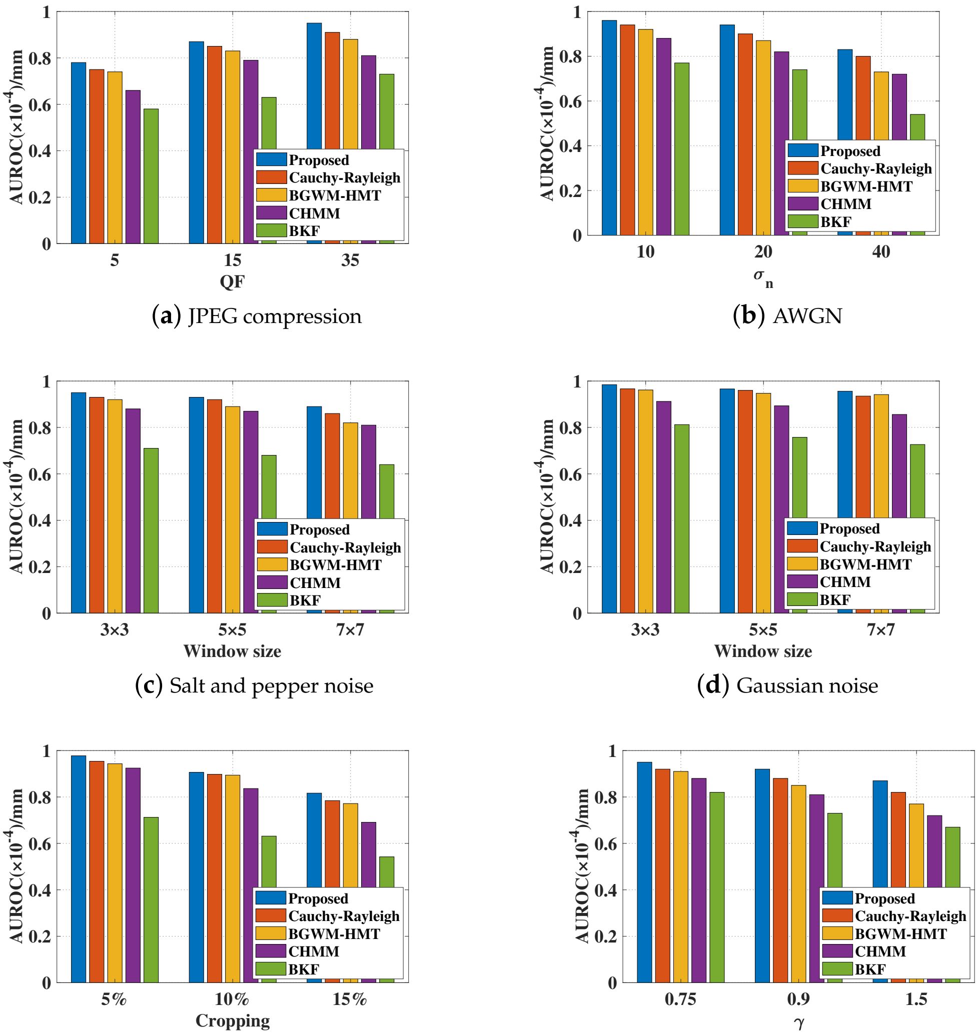

(**a**) JPEG compression (**b**) AWGN (**c**) Salt and pepper noise (**d**) Gaussian noise (**e**) Cropping (**f**) Gamma correction

Figure 10. The AUROC values corresponding to different schemes under various attacks.

Based on the above experimental results, it is evident that the proposed detector showed excellent resistance to various attacks at different WDR values. These results validate the effectiveness and robustness of the detector proposed in this paper.

Based on the above detailed comparison results, it can be concluded that the BKF–Rayleigh distribution-based watermarking detector proposed in this paper exhibited superior performance compared to existing methods. The contributions and improvements of this paper can be summarized into four main aspects: Firstly, this paper utilized local FAPHFM magnitudes in statistical image watermarking to embed the watermarking information, which could enhance the robustness of the carrier against various attacks. Secondly, BKF–Rayleigh distribution modeling was proposed to accurately model the local FAPHFM magnitudes, which could accurately capture the non-Gaussian and heavy-tailed statistical features of the local FAPHFM magnitudes and thus improve the detection performance. Thirdly, MMLE based on the RSS parameter estimation method was adopted in this paper, which could accurately estimate the statistical model parameters of BKF–Rayleigh distribution. Finally, a new blind statistical watermark detector was developed using BKF–Rayleigh distribution and the LO decision criterion. The detector performed well in detecting watermark information.

8. Conclusions

In this paper, we proposed a new watermarking algorithm to fit the amplitude coefficients of FAPHFMs with the BKF–Rayleigh distribution model and design an optimal watermark detector. Firstly, the multiplicative function was used to embed the watermark information into the FAPHFM magnitude coefficients. Secondly, in order to realize an accurate statistical modeling process, a BKF–Rayleigh-based statistical modeling method was proposed, which could accurately capture the non-Gaussian distribution characteristics of the FAPHFM magnitude values. Thirdly, MMLE based on the RSS method was chosen to solve the model parameter estimation problem effectively. Finally, an optimal blind watermark detector based on the BKF–Rayleigh model was designed using the LO decision criterion. The experimental results showed that our detector outperformed the existing watermark detection methods in terms of accuracy, imperceptibility, robustness, watermark capacity, and time complexity.

In addition, in real life, color images are very common and widespread. In the future, we will extend our algorithm to color images to provide greater convenience for copyright owners. Future research will also focus on exploring and investigating more accurate models and improving the accuracy of parameter estimation for better watermark detectors.

Author Contributions: Conceptualization, S.Y.; writing—original draft preparation, S.Y.; writing—review and editing, S.Y. and H.C.; visualization, S.Y.; supervision, A.D.; project administration, A.D. All authors have read and agreed to the published version of the manuscript.

Funding: This research received no external funding.

Institutional Review Board Statement: Not applicable.

Informed Consent Statement: Not applicable.

Data Availability Statement: Data are contained within the article.

Conflicts of Interest: The authors declare no conflict of interest.

References

1. Zhang, X.; Zhang, W.; Sun, W.; Sun, X.; Jha, S.K. A robust 3-D medical watermarking based on wavelet transform for data protection. *Comput. Syst. Sci. Eng.* **2022**, *41*, 1043–1056. [CrossRef]
2. Tavakoli, A.; Honjani, Z.; Sajedi, H. Convolutional neural network-based image watermarking using discrete wavelet transform. *Int. J. Inf. Technol.* **2023**, *15*, 2021–2029. [CrossRef]
3. Begum, M.; Ferdush, J.; Uddin, M.S. A hybrid robust watermarking system based on discrete cosine transform, discrete wavelet transform, and singular value decomposition. *J. King Saud-Univ.-Comput. Inf. Sci.* **2022**, *34*, 5856–5867. [CrossRef]
4. Dong, L.; Yan, Q.; Lv, Y.; Deng, S. Full band watermarking in DCT domain with Weibull model. *Multimed. Tools Appl.* **2017**, *76*, 1983–2000. [CrossRef]
5. Thanki, R.; Kothari, A.; Trivedi, D. Hybrid and blind watermarking scheme in DCuT–RDWT domain. *J. Inf. Secur. Appl.* **2019**, *46*, 231–249. [CrossRef]
6. Sharma, N.K.; Kumar, S.; Rajpal, A.; Kumar, N. MantaRayWmark: An image adaptive multiple embedding strength optimization based watermarking using Manta Ray Foraging and bi-directional ELM. *Expert Syst. Appl.* **2022**, *200*, 116860. [CrossRef]
7. Luo, Y.; Li, L.; Liu, J.; Tang, S.; Cao, L.; Zhang, S.; Qiu, S.; Cao, Y. A multi-scale image watermarking based on integer wavelet transform and singular value decomposition. *Expert Syst. Appl.* **2021**, *168*, 114272. [CrossRef]
8. Hu, F.; Cao, H.; Chen, S.; Sun, Y.; Su, Q. A robust and secure blind color image watermarking scheme based on contourlet transform and schur decomposition. *Vis. Comput.* **2022**, *39*, 4573–4592. [CrossRef]
9. Wang, X.; Zhang, S.; Wang, L.; Yang, H.; Niu, P. Locally optimum image watermark decoder by modeling NSCT domain difference coefficients with vector based cauchy distribution. *J. Vis. Commun. Image Represent.* **2019**, *62*, 309–329. [CrossRef]
10. Hamza, Y.A.; Tewfiq, N.E.; Ahmed, M.Q. An enhanced approach of image steganographic using discrete shearlet transform and secret sharing. *Baghdad Sci. J.* **2022**, *19*, 197–207. [CrossRef]
11. Wang, X.; Shen, X.; Niu, P.; Yang, H. BGGMM-HMT based locally optimum image watermark detector in high-order NSST difference domain. *J. Vis. Commun. Image Represent.* **2022**, *83*, 103450. [CrossRef]
12. Alghoniemy, M.; Tewfik, A.H. Image watermarking by moment invariants. In Proceedings of the Proceedings 2000 International Conference on Image Processing (Cat. No. 00CH37101), Vancouver, BC, Canada, 10–13 September 2000; Volume 2, pp. 73–76.
13. Wang, X.; Niu, P.; Tian, J.; Tian, J. A new statistical image watermark detector in RHFMs domain using beta-exponential distribution. *Soft Comput.* **2022**, *26*, 9707–9727. [CrossRef]

14. Zebbiche, K.; Khelifi, F.; Loukhaoukha, K. Robust additive watermarking in the DTWCT domain based on perceptual masking. *Multimed. Tools Appl.* **2018**, *77*, 21281–21304. [CrossRef]
15. Hamidreza, S.; Ahmad; Omair, M.; Shanmukha, S.M.N. Optimum multiplicative watermark detector in contourlet domain using the normal inverse Gaussian distribution. In Proceedings of the 2015 IEEE International Symposium on Circuits and Systems (ISCAS), Lisbon, Portugal, 24–27 May 2015; pp. 1050–1053.
16. Yakoh, T.; Oi, M. Re-shooting resistant blind watermarking framework based on feature separation with gaussian mixture model. *IEEJ Trans. Electr. Electron. Eng.* **2022**, *17*, 556–565. [CrossRef]
17. Wang, X.; Zhang, S.; Wen, T.; Xu, H.; Yang, H. Synchronization correction-based robust digital image watermarking approach using bessel k-form PDF. *Pattern Anal. Appl.* **2020**, *23*, 933–951. [CrossRef]
18. Liu, Y.; Zhang, S.; Yang, J. Color image watermark decoder by modeling quaternion polar harmonic transform with BKF distribution. *Signal Process. Image Commun.* **2020**, *88*, 115946. [CrossRef]
19. Etemad, S.; Amirmazlaghani, M. A new multiplicative watermark detector in the contourlet domain using t location-scale distribution. *Pattern Recognit.* **2018**, *77*, 99–112. [CrossRef]
20. Jiang, M.; Feng, X.; Wang, C.; Fan, X.; Zhang, H. Robust color image watermarking algorithm based on synchronization correction with multi-layer perceptron and cauchy distribution model. *Appl. Soft Comput.* **2023**, *140*, 110271. [CrossRef]
21. Ahmaderaghi, B.; Kurugollu, F.; Rincon, J.M.D.; Bouridane, A. Blind image watermark detection algorithm based on discrete shearlet transform using statistical decision theory. *IEEE Trans. Comput. Imaging* **2018**, *4*, 46–59. [CrossRef]
22. Sedighi, V.; Fridrich, J.; Cogranne, R. Content-adaptive pentary steganography using the multivariate generalized gaussian cover model. In *Media Watermarking, Security, and Forensics 2015*; SPIE: Philadelphia, PA, USA, 2015; Volume 9409, pp. 144–156.
23. Al-Wesabi, F.N. A smart English text zero-watermarking approach based on third-level order and word mechanism of Markov model. *Comput. Mater. Contin.* **2020**, *65*, 1137–1156. [CrossRef]
24. Amini, M.; Sadreazami, H.; Ahmad, M.O.; Swamy, M. A channel-dependent statistical watermark detector for color images. *IEEE Trans. Multimed.* **2018**, *21*, 65–73. [CrossRef]
25. Wang, X.; Wen, T.; Wang, L.; Niu, P. Yang, H. Contourlet domain locally optimum image watermark decoder using cauchy mixtures based vector HMT model. *Signal Process. Image Commun.* **2020**, *88*, 115972. [CrossRef]
26. Amirmazlaghani, M. Additive watermark detection in the wavelet domain using 2D-GARCH model. *Inf. Sci.* **2016**, *370*, 1–17. [CrossRef]
27. Xia, Z.; Wang, C.; Li, Y.; Yu, B.; Zhang, Y.; Li, Q.; Wang, X.; Ma, B. Geometrical attacks resilient statistical watermark decoder using polar harmonic Fourier moments. *J. Frankl. Inst.* **2023**, *360*, 4493–4518. [CrossRef]
28. Yang, H.; Wei, T.; Shen, Y.; Niu, P. Wang, X. Vector SENM-HMT-based statistical watermark decoder in NSST–PLCT magnitude domain. *Circuits Syst. Signal Process.* **2023**, *42*, 3926–3962. [CrossRef]
29. Wang, X.; Ma, R.; Shen, Y.; Niu, P. Image watermarking using DNST-PHFMs magnitude domain vector AGGM-HMT. *J. Vis. Commun. Image Represent.* **2023**, *91*, 10377. [CrossRef]
30. Shaik, A.; V, M. A robust multiplicative watermarking technique for digital images in curvelet domain using normal inverse Gaussian distribution. *Multimed. Tools Appl.* **2023**, *82*, 9223–9241. [CrossRef]
31. Sanivarapu, P.V. Adaptive tamper detection watermarking scheme for medical images in transform domain. *Multimed. Tools Appl.* **2022**, *81*, 11605–11619. [CrossRef]
32. Hu, Y.; Lu, W.; Wei, J.; Xu, J.; Ma, M. A watermark detection scheme based on non-parametric model applied to mute machine voice. *Multimed. Tools Appl.* **2023**, 1–20. [CrossRef]
33. Bi, H.; Liu, Y.; Wu, M.; Ge, Y. NSCT domain additive watermark detection using RAO hypothesis test and cauchy distribution. *Math. Probl. Eng.* **2016**, *2016*, 4065215. [CrossRef]
34. Sadreazami, H.; Ahmad, M.O.; Swamy, M.S. A robust multiplicative watermark detector for color images in sparse domain. *IEEE Trans. Circuits Syst. II Express Briefs* **2015**, *62*, 1159–1163. [CrossRef]
35. Chen, S.-T.; Hsu, C.-Y.; Huang, H.-N. Wavelet-domain audio watermarking using optimal modification on low-frequency amplitude. *IET Signal Process.* **2015**, *9*, 166–176. [CrossRef]
36. Devi, K.J.; Singh, P.; Dash, J.K.; Thakkar, H.K.; Santamaría, J.; Krishna, M.V.J.; Romero, M.A. A new robust and secure 3-level digital image watermarking method based on G-BAT hybrid Optimization. *Mathematics* **2022**, *10*, 3015. [CrossRef]
37. Juarez-Sandoval, O.U.; Garcia-Ugalde, F.J.; Cedillo-Hernandez, M.; Ramirez-Hernandez, J.; Hernandez-Gonzalez, L. Imperceptible–visible watermarking to information security tasks in color imaging. *Mathematics* **2021**, *9*, 2374. [CrossRef]
38. Gong, L.; Tian, C.; Zou, W.; Zhou, N. Robust and imperceptible watermarking scheme based on Canny edge detection and SVD in the contourlet domain. *Multimed. Tools Appl.* **2021**, *80*, 439–461. [CrossRef]
39. Niu, P.; Wang, L.; Tian, J.; Zhang, S.; Wang, X. A statistical color image watermarking scheme using local QPCET and Cauchy–Rayleigh distribution. *Circuits Syst. Signal Process.* **2021**, *40*, 4516–4545. [CrossRef]
40. Huang, T.; Xu, J.; Yang, Y.; Han, B. Robust zero-watermarking algorithm for medical images using double-tree complex wavelet transform and Hessenberg decomposition. *Mathematics* **2022**, *10*, 1154. [CrossRef]
41. Mun, S.-M.; Nam, S.-H.; Jang, H.; Kim, D.; Lee, H.-K. Finding robust domain from attacks: A learning framework for blind watermarking. *Neurocomputing* **2019**, *337*, 191–202. [CrossRef]
42. Deeba, F.; Kun, S.; Dharejo, F.A.; Langah, H.; Memon, H. Digital watermarking using deep neural network. *Int. J. Mach. Learn. Comput.* **2020**, *10*, 277–282. [CrossRef]

43. Pavlović, K.; Kovačević, S.; Djurović, I.; Wojciechowski, A. Robust speech watermarking by a jointly trained embedder and detector using a DNN. *Digit. Signal Process.* **2022**, *122*, 103381. [CrossRef]
44. Hosny, K.M.; Darwish, M.M.; Fouda, M.M. Robust color images watermarking using new fractional-order exponent moments. *IEEE Access* **2021**, *9*, 47425–47435. [CrossRef]
45. Wang, C.; Zhang, Q.; Ma, B.; Xia, Z.; Li, J.; Luo, T.; Li, Q. Light-field image watermarking based on geranion polar harmonic Fourier moments. *Eng. Appl. Artif. Intell.* **2022**, *113*, 104970. [CrossRef]
46. Gong, L.; Luo, H. Dual color images watermarking scheme with geometric correction based on quaternion FrOOFMMs and LS-SVR. *Opt. Laser Technol.* **2023**, *167*, 109665. [CrossRef]
47. Yamni, M.; Karmouni, H.; Sayyouri, M.; Qjidaa, H. Image watermarking using separable fractional moments of Charlier–Meixner. *J. Frankl. Inst.* **2021**, *358*, 2535–2560. [CrossRef]
48. Wang, H.; Chen, Y.; Zhao, T. Modified Zernike moments and its application in geometrically resilient image zero-watermarking. *Circuits Syst. Signal Process.* **2022**, *41*, 6844–6861. [CrossRef]
49. Yang, S.; Deng, A. Fast and accurate computation of polar harmonic Fourier moments for image description. *JOSA A* **2023**, *40*, 1714–1723. [CrossRef]
50. Fadili, J.M.; Boubchir, L. Analytical form for a Bayesian wavelet estimator of images using the Bessel K form densities. *IEEE Trans. Image Process.* **2005**, *14*, 231–240. [CrossRef]
51. Hoffman, D.; Karst, O.J. The theory of the Rayleigh distribution and some of its applications. *J. Ship Res.* **1975**, *19*, 172–191. [CrossRef]
52. Zheng, G.; Al-Saleh, M.F. Modified maximum likelihood estimators based on ranked set samples. *Ann. Inst. Stat. Math.* **2002**, *54*, 641–658. [CrossRef]
53. Bhinder, P.; Singh, K.; Jindal, N. Image-adaptive watermarking using maximum likelihood decoder for medical images. *Multimed. Tools Appl.* **2018**, *77*, 10303–10328. [CrossRef]
54. Koen, J.D.; Barrett, F.S.; Harlow, I.M.; Yonelinas, A.P. The ROC Toolbox: A toolbox for analyzing receiver-operating characteristics derived from confidence ratings. *Behav. Res. Methods* **2017**, *49*, 1399–1406. [CrossRef]
55. Amini, M.; Sadreazami, H.; Ahmad, M.O.; Swamy, M. Multichannel color image watermark detection utilizing vector-based hidden Markov model. In Proceedings of the 2017 IEEE International Symposium on Circuits and Systems (ISCAS), Baltimore, MD, USA, 28–31 May 2017; pp. 1–4.
56. Mareen, H.; Van Kets, N.; Lambert, P.; Van Wallendael, G. Fast fallback watermark detection using perceptual hashes. *Electronics* **2021**, *10*, 1155. [CrossRef]
57. Faheem, Z.B.; Ishaq, A.; Rustam, F.; de la Torre Díez, I.; Gavilanes, D.; Vergara, M.M.; Ashraf, I. Image watermarking using least significant bit and canny edge detection. *Sensors* **2023**, *23*, 1210. [CrossRef]
58. Pourhashemi, S.M.; Mosleh, M.; Erfani, Y. A novel audio watermarking scheme using ensemble-based watermark detector and discrete wavelet transform. *Neural Comput. Appl.* **2021**, *33*, 6161–6181. [CrossRef]
59. Wang, X.; Shen, X.; Tian, J.; Niu, P.; Yang, H. Locally optimum image watermark detector based on statistical modeling of SWT-EFMs magnitudes. *J. Inf. Secur. Appl.* **2022**, *65*, 103105. [CrossRef]